

# Bound in the continuum modes in indirectly-patterned hyperbolic media

**Frank Koppens** (✉ [frank.koppens@icfo.eu](mailto:frank.koppens@icfo.eu))

ICFO - The Institute of Photonic Sciences <https://orcid.org/0000-0001-9764-6120>

**Hanan Herzig-Sheinfux**

Institute of Photonic Sciences

**Lorenzo Orsini**

ICFO - The Institute of Photonic Sciences

**Minwoo Jung**

Cornell University <https://orcid.org/0000-0001-6985-2293>

**Iacopo Torre**

ICFO - The Institute of Photonic Sciences <https://orcid.org/0000-0001-6515-181X>

**Matteo Ceccanti**

ICFO - The Institute of Photonic Sciences

**Rinu Maniyara**

ICFO - The Institute of Photonic Sciences

**David Barcons-Ruiz**

Institute of Photonic Sciences

**Sebastian Castilla**

ICFO - The Institute of Photonic Sciences

**Niels Hesp**

ICFO - The Institute of Photonic Sciences <https://orcid.org/0000-0001-8111-9780>

**Eli Janzen**

Kansas State University

**Valerio Pruneri**

ICFO-The Institute of Photonic Sciences <https://orcid.org/0000-0002-6425-9332>

**James Edgar**

Kansas State University <https://orcid.org/0000-0003-0918-5964>

**Gennady Shvets**

Cornell University

---

Physical Sciences - Article

**Keywords:** nanoscience, bound state in continuum (BIC) cavities

**Posted Date:** April 8th, 2021

**DOI:** <https://doi.org/10.21203/rs.3.rs-385236/v1>

**License:**  This work is licensed under a Creative Commons Attribution 4.0 International License.

[Read Full License](#)

---

## Bound in the continuum modes in indirectly-patterned hyperbolic media

**Authors:** Hanan Herzig Sheinfux<sup>1</sup>, Lorenzo Orsini<sup>1</sup>, Minwoo Jung<sup>2</sup>, Iacopo Torre<sup>1</sup>, Matteo Ceccanti<sup>1</sup>, Rinu Maniyara<sup>1</sup>, David Barcons Ruiz<sup>1</sup>, Sebastian Castilla<sup>1</sup>, Niels C.H. Hesp<sup>1</sup>, Eli Janzen<sup>3</sup>, Valerio Pruneri<sup>1</sup>, James H. Edgar<sup>3</sup>, Gennady Shvets<sup>4</sup>, Frank H.L. Koppens<sup>1,5</sup>

<sup>1</sup> ICFO-Institut de Ciències Fòniques, 08860 Castelldefels (Barcelona), Spain

<sup>2</sup> Department of Physics, Cornell University, Ithaca, New York, 14853, USA

<sup>3</sup> Department of Chemical Engineering, Kansas State University, Durland Hall, Manhattan, KS 66506-5102, USA

<sup>4</sup> School of Applied and Engineering Physics, Cornell University, Ithaca, New York 14853, USA

<sup>5</sup> ICREA-Institució Catalana de Recerca i Estudis Avançats, 08010 Barcelona, Spain

**A conventional optical cavity supports one or more modes, which are confined since they are unable to leak out of the cavity. Bound state in continuum (BIC) cavities are an unconventional alternative, based on confinement by destructive interference<sup>1,2</sup>, even though optical leakage channels are available. BICs are a general wave phenomenon<sup>2-8</sup>, of particular interest to optics<sup>6,9-14</sup>, but BICs have never been demonstrated at the nanoscale level. Nanoscale BIC cavities are more challenging to realize, however, as they require destructive interference at the nanometer scale. Here, we demonstrate the first nanophotonic cavities based on BIC and find an unprecedented combination of quality factors and ultrasmall mode volume. In particular, we exploit hyperbolic media, HyM, as they can support large (in principle unlimited) momentum excitations, which propagate as ultra-confined rays, so that HyM cavities can in principle be extremely small. However, building a hyperbolic BIC (hBIC) cavity presents a fundamental challenge: an hBIC has an infinite number of modes, which would all need to interfere simultaneously. Here, we bring the BIC concept to the nanoscale by introducing and demonstrating a novel multimodal reflection mechanism of the ray-like optical excitations in hyperbolic materials. Using near-field microscopy, we demonstrate mid-IR confinement in BIC-based nanocavities with volumes down to  $23 \times 23 \times 3 \text{ nm}^3$  and quality factors above 100 – a dramatic improvement in several metrics of confinement. This alliance of HyM with BICs yields a radically novel way to confine light and is expected to have far reaching consequences wherever strong optical confinement is utilized, from ultra-strong light-matter interactions, to mid-IR nonlinear optics and a range of sensing applications.**

The general premise of nanophotonics involves shrinking light to the subwavelength nanometric scale, for example by compressing light into the tiny volume of a nanocavity which dramatically enhances its interaction with matter. Innovations in nanocavity design<sup>15</sup> have allowed even single emitters to be strongly bound to cavity polaritons<sup>16-18</sup>. Likewise, nanocavity coupling strengths can become so large as to reach the onset of ultrastrong<sup>19</sup> and deep<sup>20</sup> coupling regimes, where bound states entangle with virtual excitations<sup>21,22</sup>, challenging the basic understanding of light matter interaction. However, shrinking light typically comes at a cost – absorption losses, which plague all existing nanocavity designs. Fig. 1a visually summarizes the state of the art in nanocavity research<sup>23-36</sup> and shows that cavity performance progressively worsens beneath the 100 nm scale (i.e. for  $V < 10^{-4} \lambda_0^3$ , with  $\lambda_0$  the

vacuum wavelength). Virtually all cavities in that regime show low  $Q$ -factors, on the order of ten or less. Moreover, unlike the intuitive interpretation for ordinary optical cavities, the  $Q$ -factor of a nanocavity is not the number of times light cycles in the nanocavity. On the nanoscale, light tends to travel slower and light in a  $Q = 10$  nanocavity may only complete 2-3 cycles in the cavity. Indeed, slow light effects rather than interference become the dominant contribution to the quality factor in the smallest plasmonic cavities<sup>37</sup>.

A possible route to strong nanoscale confinement lies with hyperbolic Phonon polaritons (PhPs), which can exhibit very high momenta modes. As shown in Fig. 1a, cavities with  $Q > 200$  and of sizes of  $\sim 300$  nm have been demonstrated<sup>38-47</sup>. However, further size reduction is inhibited by the intrinsic nanoscale damage made in making a cavity with the conventional cavity design. This motivates the exploration of indirectly patterned concepts, which do not incur any damage to the hBN, at any size scale and makes a BIC-like approach an appealing candidate. Typically a BIC has tunable parameters or symmetries that can force interference between  $\sim 2$  channels of leakage<sup>2</sup>. But since a HyM supports a large (theoretically infinite) number of modes inside and outside of the cavity, making a hyperbolic BIC requires a mechanism that will make tuning possible between a large number of modes.

Here, we introduce a new class of cavities and combine BICs and HyMs for the first time, demonstrating the previously unattainable fusion of high-quality factors with ultra-small modal volumes. Confinement in our hBIC cavities stems from a unique multimodal reflection enhancement mechanism, which is intimately related to the ray-like nature of excitations in HyM<sup>39,48,49</sup>. It is this ray-like nature that allows hBICs to be fully compact in 3D and to remain confined in the presence of an infinite number of leakage channels. Using scattering-type near-field microscopy<sup>50,51</sup> (SNOM), we directly observe this reflection enhancement mechanism and demonstrate the previously unattainable  $Q > 100$  in a cavity size  $< 100$  nm and with mode volume confinement above  $10^9$ . Notably, such high performance cannot be explained in the absence of BIC-like multimodal interference effects.

Consider first a slab of HyM on a flat dielectric substrate. Unlike a regular dielectric, there are many modes in a HyM slab (regardless of its thickness). Placing a dipole source on the slab excites a superposition of the eigenmodes in the slab, as shown in Fig. 1b and denoted by  $A_0, A_1, \dots$ . This superposition forms a TM polarized ray-like excitation, as illustrated in Fig. 1c, whose electric field is strongly concentrated with a Lorentzian profile much narrower than the free-space wavelength (see<sup>52</sup>). The Lorentzian-profiled ray propagates at a fixed angle  $\pm \text{atan}\left(\frac{L_{ray}}{t}\right)$  inside the flake. As it propagates, it broadens as  $\Gamma \simeq \text{imag}\left(\sqrt{-\frac{\epsilon_x}{\epsilon_z}}\right) x$  (see Fig. 2a). Due to its ray-like nature, this multimodal excitation does not accumulate phase by continuous propagation. Rather, the ray gains phase at discrete jumps at every internal reflection, gaining the complex phase from  $r$  at every jump.

An intriguing scenario occurs if this ray is incident exactly on the corner of a metallic structure. Above a metallic substrate, the electric field of the eigenmodes  $M_1, M_2, \dots$  is zero at the hBN-metal interface due to the screening (see Fig. 1c). Since the ray is narrow (in an ideal lossless HyM, it is infinitesimally narrow and in practice it is  $1 - 2$  nm in a 25 nm thick flake) the overlap with any of the modes  $M_1, M_2, \dots$  is very small and the reflection is greatly enhanced. Specifically, for  $t \gg \Gamma$ , the reflection coefficient can be written<sup>52</sup> as  $r = 1 - \delta$ , with  $\delta$  proportional  $\Gamma/t$ . Hence, the narrower the beam is, the closer the reflection is to unity and in an ideal HyM, it is perfect. Now, if the cavity width is such that the ray travels from one metallic corner to the other (i.e. it is an integer multiple of  $L_{ray}$ ), it can be contained inside the cavity, despite the abundance of a continuum of modes outside the cavity. Intriguingly, the

reflection mechanism which enables hBIC formation can be understood as destructive interference with a spatial origin that occurs on an infinite number of modes simultaneously.

The hBIC cavities we propose consist of a sharply defined hole (with nanometer sharp corners) in a gold film covered by a thin flake of hexagonal Boron Nitride (hBN), which supports PhPs in its Reststrahlen bands<sup>53–57</sup>. For a mode to form, the ray needs to acquire an integer multiple of  $2\pi$  phase, in addition to the aforementioned geometric condition (the ray bouncing from one corner to the other). The hBIC existence conditions are depicted in Fig. 2b, which shows the condition for perfect reflection and the phase accumulated by the ray (in a 25nm thick flake on top of a 100nm wide trench). Every black circle in Fig. 2b represents a ray which completes  $n_s$  bounces (with  $n_s \in \mathbb{N}$ ), is perfectly reflected, and accumulated a multiple of  $2\pi$  phase in every roundtrip. These modes are also apparent in an independent semi-analytical model of the 1D cavity, based on the Schwartz decomposition<sup>58</sup>. This model allows an explicit separation of the cavity response from the response of the bare hBN slab and, as seen in Fig. 2c, also shows modes forming with resonant frequency and width similar to those extracted otherwise.

Intriguingly, hBICs can be compact in all three dimensions, which is understood to be impossible in non-hyperbolic media<sup>59</sup>. This exceptional property is a consequence of the infinite momentum associated with the ray-like hBICs. When absorption is included into the model, ray broadening diminishes the reflection and reduces the quality factor. In Fig. 2a, we consider the effect of loss explicitly – we approximate the quality factor of a trench-like cavity as a function of the loss factor  $\alpha$  which multiplies the imaginary part of the permittivity (i.e.  $\epsilon_{x,z} \rightarrow \text{real}(\epsilon_{x,z}) + \alpha \cdot \text{imag}(\epsilon_{x,z})$ ). When the loss factor approaches zero,  $Q$  diverges, showing this is indeed a proper mode despite being bound in continuum. In the presence of finite losses, the quality factor is limited, but much larger than it would have been without multimodal interference. Indeed, as we show next, BIC-like multimodal interference continues to play an essential role in the confinement of light in our nanocavities.

The hBIC cavity is fabricated from an ultrathin and ultra flat layer of 10nm gold (with a 2nm Ti sticking layer, roughness  $< 0.5\text{nm rms}$ ) evaporated on a silica substrate<sup>67</sup>. The gold layer is patterned using a focused Ne ion beam, giving a minimal feature size of about 6nm. A mechanically exfoliated isotopically pure hBN flake<sup>60</sup> is then transferred on top of the patterned gold. The ultra-flatness of the gold allows us to keep the pristine quality of an isotopic hBN flake (known to support exceptionally long PhP lifetimes<sup>46,47,57</sup>). It should be emphasized that both the quality of the flakes and the exceptional resolution of Ne ion milling are instrumental to the success of the measurements reported here.

We begin our investigation of these cavities with the instructive case of a single “reflector”: an hBN flake which is half-suspended from a metallic surface (see Fig. 1c). The tip of our scattering-type near field microscope acts similarly to a dipole source, launching a multimodal ray-like beam which reflects from the edge of the trench where the substrate changes from air to metal. As the tip scans across the edge, we observe interference fringes whenever the PhPs launched by the tip constructively interfere with their reflection from the trench’s edge (Fig. 3a). The dashed white lines indicate the fitted locations of the relatively faint interference fringe maxima associated with the  $M_1$  modes. Likewise, the dashed black lines correspond to the expected interference fringes associated to the  $A_0$  mode, which is experimentally barely visible. However, the most prominent feature of Fig. 3a is the strong fringe seen on the suspended hBN side only. This strong fringe can be associated with the expected ray location – the dashed green line – and not any of the PhP modes,  $A_0$ ,  $A_1$  or  $M_1$ . This asymmetry in the reflection is expected for a ray-like excitation<sup>52</sup>, but is in stark contrast with the naïve single mode theory (i.e. neglecting high order modes) where the reflection amplitude should be

symmetric. To quantify the reflection asymmetry, we show in Fig. 3b the ratio of the ray-like reflection amplitude to the  $M_1$  reflection amplitude, which is expected to be unity if only single mode reflections take place.

The full cavity consists of a slab of suspended hBN, which is fully surrounded by reflecting metallic corners (inset of Fig. 4a). We consider two cavity sets: C1 with a thicker 25nm flake of hBN and C2 with a thinner 3nm flake (the momentum of hBN PhPs scales with  $1/t$ , so thinner flakes can support smaller cavities). The near-field signal measured from a representative 250x250nm<sup>2</sup> square cavity in the C1 set is shown in Fig. 4b for a number of frequencies. This signal represents the spatial distribution of the (projected) local density of states (see SI) and shows a clear evolution with frequency: first rising and then receding in amplitude, in both the experiment and in finite element simulations, also shown in Fig. 4b. The mode profile suggests that this is the lowest order cavity mode and the fast rate of change (within 10s of cm<sup>-1</sup>) suggests that the quality factor is high. Repeating this measurement for a set of cavities with different widths, we obtain Fig. 4c, which shows the normalized near-field signal in the middle of the cavity as a function of frequency and cavity width. The width of the cavities roughly corresponds to  $\lambda_{A_0}/2$ , as expected because a  $\lambda_{A_0}/2$  sized cavity is resonant for both cases of single mode and multimodal confinement. This is because the total rate of phase accumulation for the ray is the same as the  $A_0$  mode<sup>61</sup>.

As the cavity shrinks, the signal strength becomes weaker since the near-field microscope picks up less signal, but the resonances in Fig. 4c (and simulations in 4d) exhibit little broadening, suggesting the quality factor is maintained. In fact, the signal reduction witnessed in the experiment is primarily due to the tip drifting (mechanically) away from the cavity during the frequency sweep. To circumvent this drift problem, we applied a pseudo-heterodyne near-field measurement for a fixed frequency in order to obtain the complex amplitude and phase. From these data, we extracted the optical phase as a function of the cavity width, as shown in Fig. 5a. The measured data show a clear  $\pi$ -phase jump, as expected when changing a critical parameter across a resonance. This phase-response in cavity set C1 can be clearly identified and quantified for cavities down to 60x60nm<sup>2</sup>. To shrink the cavity size further, we turn to cavity set C2, where the hBN is even thinner at 3nm and where even finer cavities are made with diameters down to  $\sim 6$ nm. These very small cavities show in general a weaker signal, which complicates the measurement (see extended data in SI). We can nevertheless identify the cavity response down to a cavity volume of  $23 \times 23 \times 3$ nm<sup>3</sup>, including the phase jump at the resonant frequency (Fig. 5b).

The question arises: what is the smallest cavity size that can be produced using these techniques? Remarkably, the limitation on cavity size in our experiments is not fundamental, i.e., nonlocality in the PhP dispersion, but technological. Specifically, while the gold layer we use is very flat, the nano-landscape shows typical features,  $< 1$ nm tall and 5 – 15nm wide. These features generate a background signal comparable to the signature of the smallest nanocavities, complicating the measurement and obfuscating the real cavities. Regarding fabrication quality, it is interesting to note that intentionally reducing the fabrication quality, for example by increasing the radius of the Ne-FIB beam from  $\sim 1.5$  to 10nm, results in a dramatic change in cavity response in cavity set C1, as shown in Fig. 5c. The lineshape broadens, indicating a significantly reduced cavity performance, a trend which is replicated in COMSOL simulations (Fig. 5d). This extreme sensitivity is in itself intriguing and indicative of the sensing capabilities of such cavities. Another technological barrier to overcome has to do with near-field microscopy itself. As it stands, the field profile of the cavities in our experiments is already more than 200 times smaller than vacuum wavelength, which is the highest compression seen in an infrared near-field measurement<sup>55</sup>. Such extreme contraction implies that the coupling efficiency into the smaller nanocavity is extremely poor, because the area of the tip is several times

larger than the cavity. It is thus remarkable that any nearfield signal is observed, which we attribute to the resonant enhancement by the cavity. We conclude that reducing the cavity size below 10nm challenges the limits of fabrication and measurement, but there does not seem to be any conceptual barrier.

Having observed this strong confinement, we can now discuss its origin and the role of BIC-like multimodal effects. To evaluate the cavity performance, we extracted the  $Q$ -factor from the frequency sweep, as well as from the spatial dependence in single frequency scans. In the latter case, specifically, we obtained both phase-sensitive pseudo-heterodyne measurements, where the phase response is easier to interpret, and homodyne measurements, that give stronger signal. The measured quality factors as a function of cavity size (Fig. 5e) show record-large numbers for these small cavity volumes, and all three types of measurements yield similar values. Intriguingly, the cavity quality factor improves when the cavity size decreases. This is a counterintuitive trend, and is also not consistent with COMSOL simulations. We attribute this trend to minute details such as the effect of strain in hBN<sup>62</sup>, of roughness in the metal and of a non-spherical tip shape, which are not included in the simulations. Peak values in Fig. 4a correspond to  $Q \approx 100$  for cavity set C1 with a  $V \approx 90 \times 90 \times 25\text{nm}$  cavity volume, and  $Q \approx 125$  with a  $V \approx 100 \times 100 \times 3\text{nm}$  volume, for cavity set C2. Here, the cavity volume is the real part of mode volume obtained in a quasi-normal mode calculation (details in SI). The role of interference in this case can be quantified by the finesse  $\mathcal{F} = \frac{v_g}{v_p} Q$ , with  $v_g, v_p$  being the group and phase velocities. For the cavities in this work we find  $\mathcal{F} > 5$ , indicating that resonant interference plays the dominant role. We note that similarly high-quality factors were also found for the smallest cavities, including the  $23 \times 23\text{nm}^2$  cavity studied above. However, due to the weaker signal in that case, there is a much larger magnitude of error, making exact numbers difficult to extract, in contrast with the case of slightly larger cavities.

Crucially, the measured and simulated  $Q$  is much larger than could be expected without multimodal effects. Specifically, we calculate in the SI an upper bound on the  $Q$  of the cavity based on a single impedance mismatched mode, but, unsurprisingly, we find that impedance mismatch is a generally poor way to confine light. Denoting the wavelengths of the lowest order hBN modes on a dielectric and metallic substrate by  $\lambda_a, \lambda_m$ , the impedance mismatch for hBN modes can be calculated to be  $\frac{\lambda_{A0}}{\lambda_{M1}} = \frac{1}{2} \frac{\pi(2m-1) - \rho_r}{\pi n - \rho_r}$ , with  $\rho_r = \text{Imag}(\text{Log}(r))$ . The magnitude of  $\frac{\lambda_{A0}}{\lambda_{M1}}$  is experimentally verified by measuring and fitting the PhP dispersion and is in good agreement with theoretical expectation. While  $\frac{\lambda_{A0}}{\lambda_{M1}}$  is very significant, ranging from 3 to 10 depending on frequency, the typical quality factor we find is  $Q_{max} = 30 - 40$  (and even this number is overwhelmingly due to the slow light effect). Importantly, this single mode upper bound is notably lower than the typical cavity  $Q$  that we measure and less than half of the peak quality factor. This single mode upper bound is also seen to be about a third of the COMSOL simulation result. This type of deviation cannot be reconciled with the impedance mismatch extracted from the measurement and leads us to conclude that the single mode description is severely lacking. Additional (high order) modes improve the reflection at the cavity edges, in a manner similar to that seen with the single reflection experiment and the hBIC theory.

To conclude, we return to Fig. 1a and compare the resonators in the current work with all alternative types of nanocavities. At  $Q > 100$ , our indirectly defined cavities are orders of magnitude smaller than any other optical resonator of a comparable  $Q$ , both in absolute volume and in terms of normalized volume. This high  $Q$  (low loss) is a testament to the power of our hBIC approach including indirect patterning, which keeps the hBN pristine. Importantly, a similar fabrication approach could be elegantly applied to assemble a range of subwavelength optical devices. Moreover, the small volume

of our cavities implies a gigantic Purcell enhancement  $Q/V > 10^9 \lambda^{-3}$ , with potential for exploring new regimes of quantum light-matter interactions. Another route to exploit this Purcell enhancement is the integration with newly developed 2D infrared quantum sources<sup>63</sup> and detectors<sup>64,65</sup>. Alternatively, many of the insights of our work can be applied to hyperbolic metamaterial cavities in order to study hBICs and enhanced light matter interactions over a much broader range of frequencies, including the visible and near infrared where mature quantum technologies already exist.

## Figures:

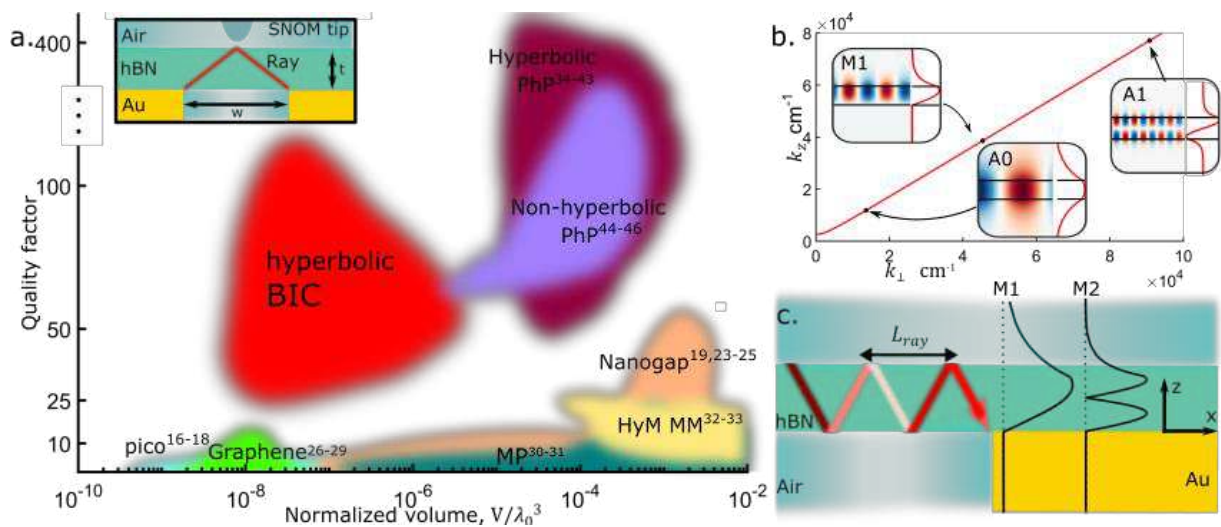


**Fig. 1, Overview of nanocavity and HyM physics.** **a.** Survey of quality factor and normalized cavity volume (normalized by the vacuum photon volume) in various types of cavities and the ones reported here. Colored areas correspond to different cavity types: picocavities (pico), nanogap plasmon polaritons (nanogap), graphene plasmon polaritons (graphene), metallic particles (MP), hyperbolic metamaterials (HyM MM), non-hyperbolic phonon polaritons and hyperbolic phonon polaritons. Hybrid cavities, i.e. plasmonic structures embedded in macro-optical resonators can show higher quality factors at relatively large volumes<sup>66</sup>, but are not shown. Generally, cavities with  $V$  below  $10^6 \text{ nm}^3$  show low quality factors, typically below 10, and always below 20. See also extended details in SI. **Inset** shows a schematic of an hBIC cavity, with a ray-like excitation (red) and a nearby near field microscope tip. **b.** The isofrequency line in momentum space for  $h^{11}\text{BN}$  at  $\omega = 1505 \text{ cm}^{-1}$ . The black dots show the location of the PhP eigenmodes A0, A1 and M1 associated to a 55nm thick flake. The PhP ray propagating in the hBN consists of a superposition of the eigenmodes A0, A1, A2,... The **Insets** show the calculated electric field distribution and profile of these eigenmodes. **c.** Illustration of ray propagation and reflection mechanism from a single cavity wall. The alternating color of the ray represents the phase of the ray, which increases at discrete jumps at every reflection from the top/bottom surfaces of the hBN. At the cavity wall, the overlap of the ray with the  $M_1, M_2$  modes (intensity profiles shown on the right) is minimal if the ray impinges exactly at the corner, leading to enhanced reflection.

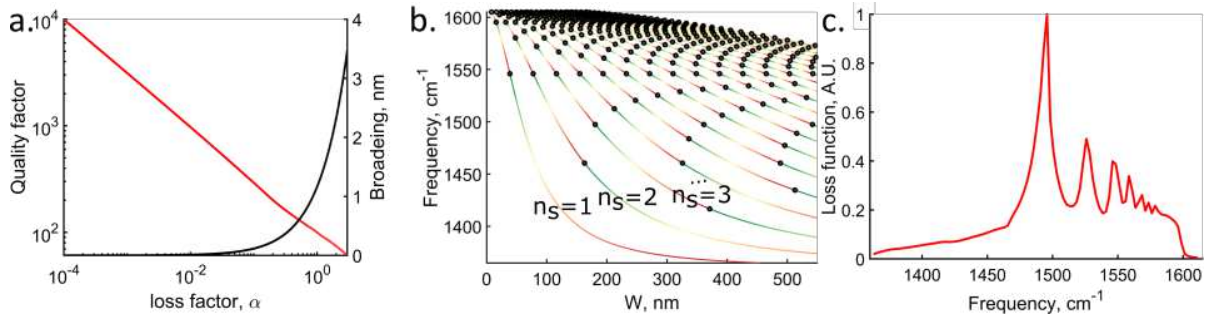


**Fig. 2, Hyperbolic bound state in continuum cavities.** **a.** Red line shows the analytical estimate of the quality factor as a function loss factor (a number multiplying the imaginary part of the model permittivity) The black line shows the broadening, in nm, incurred for a ray in one skip inside the cavity. **b.** Conditions for hBIC formation. The solid lines are labeled by an integer  $n_s$ , which is the number of skips the ray makes inside the cavity (e.g.,  $n_s = 1$  for Fig. 2a). The color of the line indicates phase accumulated in one roundtrip inside the cavity and the black dots indicate the frequency and cavity width for which a  $2\pi m$  phase is accumulated (for  $m \in \mathbb{N}$ ) and an hBIC can form. For example, the top left dot is a 1-skip cavity in which a  $2\pi$  phase is accumulated and in the top row of dots  $m = n_s$ , whereas other dots correspond to different values of  $m/n_s$  fractions **c.** Semi-analytical calculation of the loss function<sup>58</sup> in a 100nm wide cavity below a 25nm thick flake.

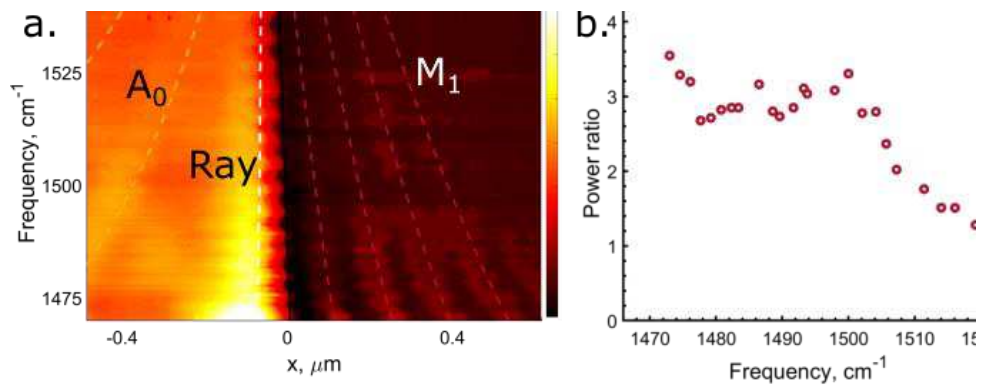


**Fig. 3, SNOM measurements of ray and mode reflections.** **a.** SNOM signal from PhPs of hBN that is placed on top of gold with a milled trench. The edge of the trench is at position  $X = 0$ , with metal below the hBN for  $x > 0$ . The trench is 800 nm wide and only the right half is shown, with the border indicated by the solid black line. The measurement shows a very strong fringe associated with the ray-like excitation and relatively faint fringes associated with M1 and A0. The dashed white line indicates the fitted location of the M1 fringes. The dashed green and red lines show the calculated location of the  $A_0$  fringes and of the ray-like excitation which reaches from the top of the flake to the metallic corner, in good agreement with experimental observation. **b.** Normalized ratio of the amplitude of the ray-like fringe to the first fringe on the metal side. This asymmetry cannot be explained if multimodal effects are not considered.

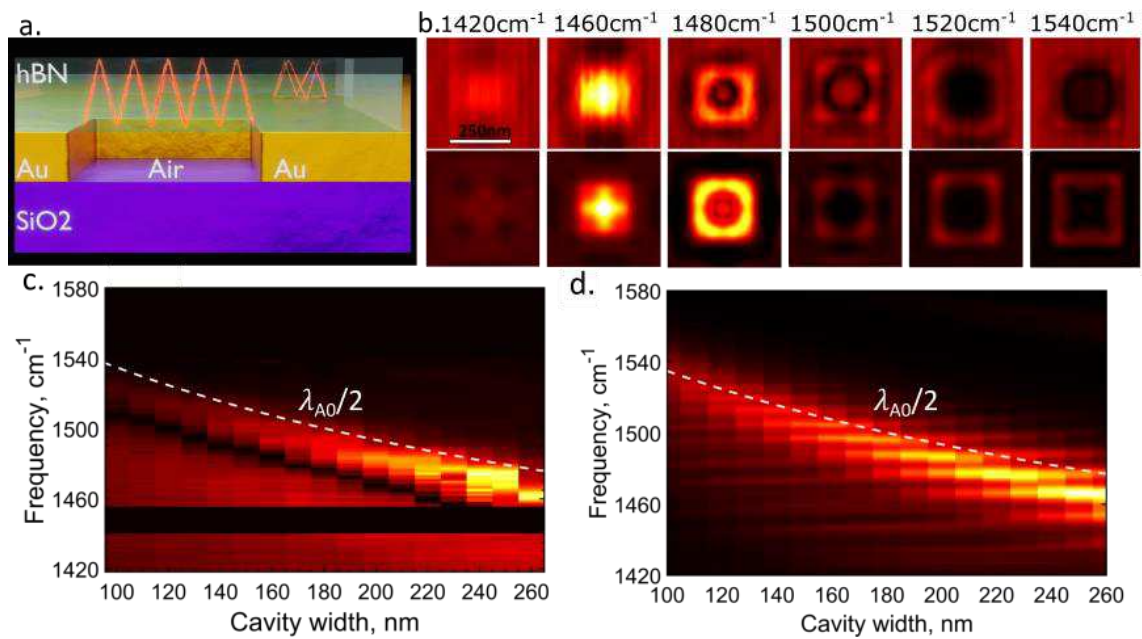


**Fig. 4, SNOM measurements of the hBIC cavities.** **a.** Illustration of two cavities and ray-like excitations in them. **b.** Measured (top) and simulated (bottom) field distribution of a single square-shaped cavity (250nmx250nm) at several frequencies. **c.&d.** Measured and simulated near-field signal in the middle of the cavity as a function of frequency and cavity size. The dashed white line on the experimental plot shows the expected first order resonance of the cavity. The undulations in the simulations are linked to multimodal beating interference, which in limit of lowering losses is expected to turn into an hBIC with  $n_s \approx 2 - 3$ .

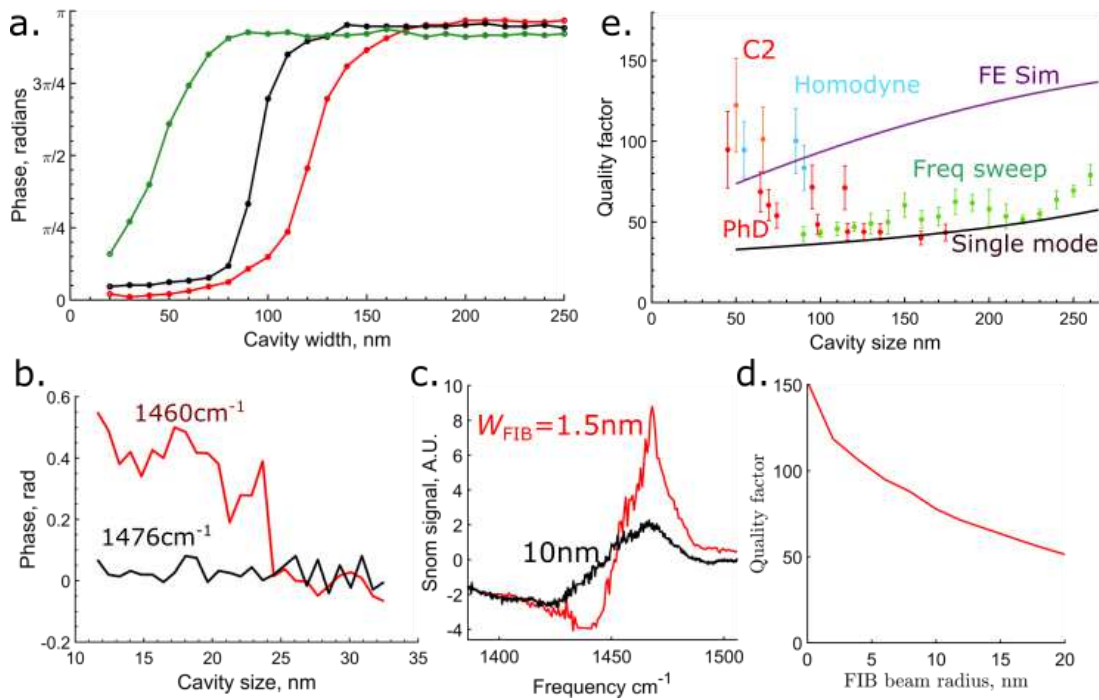


**Fig. 5, Quantifying cavity quality factors.** **a.** Measured SNOM phase as a function of cavity width for cavity C1 (25nm thick hBN flake), showing a  $\pi$  phase-jump across the resonance. **b.** Similar measurement, but for a 3nm thick flake and for a set of smaller cavities. The on-resonance signal (red line taken at  $1460\text{ cm}^{-1}$  shows a clear phase-jump, in clear contrast with the off-resonance signal (black line, at  $1476\text{ cm}^{-1}$ ). Note that the phase-jump is smaller than  $\pi$ , due to coupling inefficiency and averaging because of the small cavity size in comparison with the SNOM tip apex. **c.** Spectral response of two cavities, one milled with a sharply focused FIB beam (1.5nm radius spot size) and the other intentionally broadened (10nm radius). **d.** Simulated quality factor in cavities as a function of the milling beam's radius. **e.** Quality factor vs. cavity width measured in our experiment. The solid black line shows the theoretical upper-bound limit that can be attained by neglecting higher order modes and the purple line is a finite element simulation that includes the ray-like propagation and reflection. The measured values have been extracted by three different type of measurements (see SI): frequency sweeps (green), pseudoheterodyne scans (red for cavity set C1 and orange for cavity set C2) and homodyne amplitude scans (light blue). Different extraction methods are in general agreement and in all cases exceed the single mode theory. Theory and simulations are for a 25nm  $\text{h}^{11}\text{BN}$  flake, similar to cavity set C1.

## **Methods**

Detailed methods and extended discussion of techniques are available in the supplementary information.

### **Sample fabrication**

The cavity substrate is a Si chip with a 285nm SiO<sub>2</sub> oxide layer on which a metallic layer of 2nm Ti followed by 10nm Au layer is evaporated (Kurt J. Lesker Company – LAB 18 Thin Film Deposition System). The metallic surface is patterned using a Ne<sup>+</sup> focused ion beam (Zeiss Orion microscope) which is focused to a spot size of ~6nm, working with 5μT Ne pressure and a 10um aperture. Isotopic hBN flakes are then mechanically exfoliated and transferred onto the substrate using one of two standard techniques. Cavity C1 and the large trench are made using polydimethylsiloxane (PDMS) based exfoliation and transfer (X0 retention, DGL or PF type from Gelpak). Cavity C2 was made with a polycarbonate (PC) transfer, using homemade PC stamps. In both cases, contact mode AFM was used to clean the surface.

### **Nearfield measurements**

All measurements were performed using a commercially available scattering-type near field microscope (Neaspec), equipped with Pt coated AFM tips (Arrow NCPT from Nanoandmore, nominal diameter of 40-50nm). The laser source was a tunable quantum cascade laser (Daylight Instruments MIRcat), giving 10 to 90mW CW laser power, depending on frequency. In homodyne mode, the laser frequency was increased in small increments using a computerized interface to produce frequency sweeps and the signal at each frequency was normalized against the maximum signal measured far away from the cavities, during the exact same scan. Alternatively, single frequency scans were taken directly in either homodyne or pseudoheterodyne mode.

### **Theoretical analysis**

Theory on the formation of bound in continuum modes and evaluation of the cavities on a single mode basis is detailed in the supplementary material. All numerical calculations are made using COMSOL Multiphysics.

### **Data availability**

The data that support the findings of this study are available from the corresponding author upon request.

### **Acknowledgements**

F.H.L.K. acknowledges support by the ERC TOPONANOP under grant agreement n° 726001, the Government of Spain (FIS2016-81044; Severo Ochoa CEX2019-000910-S), Fundació Cellex, Fundació Mir-Puig, and Generalitat de Catalunya (CERCA, AGAUR, SGR 1656). Furthermore, the research leading to these results has received funding from the European Union's Horizon 2020 under grant agreement no. 881603 (Graphene flagship Core3). H.H.S. acknowledges funding from the European Union's Horizon 2020 programme under the Marie Skłodowska-Curie grant agreement Ref. 843830. N.C.H.H. acknowledges funding from the European Union's Horizon 2020 programme under the Marie Skłodowska-Curie grant agreement Ref. 665884. J.H.E. acknowledges support from the Office of Naval Research (award N00014-20-1-2474) for the hBN crystal growth is appreciated. M.J. and G.S. acknowledge the support by the Office of Naval Research (ONR) under a Grant No. N00014-21-1-2056, and by the National Science Foundation (NSF) under the Grants No. DMR-

1741788 and DMR-1719875. M.J. was also supported in part by the Kwanjeong Fellowship from Kwanjeong Educational Foundation

Contributions:

H.H.S., L.O., M.C., D.B.R, S.C., R.M., V.P. worked on sample fabrication. Isotopic hBN crystals were grown by E.J. and J.E. Measurements were performed by H.H.S and L.O. with help from D.B.R and N.C.H.H. Analytical and semi-analytical theory was developed by H.H.S., I.T. and M.C. and numerical calculations were performed by M.J. and G.S. Experiments were designed by H.H.S and F.H.L.K. All authors contributed to writing the manuscript and V.P., G.S. and F.H.L.K supervised the work.

1. von Neumann, J. & Wigner, E. P. Über das Verhalten von Eigenwerten bei adiabatischen Prozessen. in *The Collected Works of Eugene Paul Wigner* 294–297 (1993). doi:10.1007/978-3-662-02781-3\_20.
2. Hsu, C. W. *et al.* Bound states in the continuum. *Nat. Rev. Mater.* **1**, 16048 (2016).
3. González, J. W., Pacheco, M., Rosales, L. & Orellana, P. A. Bound states in the continuum in graphene quantum dot structures. *EPL (Europhysics Lett.)* **91**, 66001 (2010).
4. Guevara, M. L. L. de, Claro, F. & Orellana, P. A. Ghost Fano resonance in a double quantum dot molecule attached to leads. *Phys. Rev. B* **67**, 195335 (2003).
5. Dreisow, F. *et al.* Adiabatic transfer of light via a continuum in optical waveguides. *osapublishing.org*.
6. Plotnik, Y. *et al.* Experimental Observation of Optical Bound States in the Continuum. *Phys. Rev. Lett.* **107**, 183901 (2011).
7. Moiseyev, N. Suppression of Feshbach Resonance Widths in Two-Dimensional Waveguides and Quantum Dots: A Lower Bound for the Number of Bound States in the Continuum. *Phys. Rev. Lett.* **102**, 167404 (2009).
8. Cobelli, P. J., Pagneux, V., Maurel, A. & Petitjeans, P. Experimental observation of trapped modes in a water wave channel. *EPL (Europhysics Lett.)* **88**, 20006 (2009).
9. Watts, M. R., Johnson, S. G., Haus, H. A. & Joannopoulos, J. D. Electromagnetic cavity with arbitrary Q and small modal volume without a complete photonic bandgap. *Opt. Lett.* **27**, 1785 (2002).
10. Jin, J. *et al.* Topologically enabled ultrahigh-Q guided resonances robust to out-of-plane scattering. *Nature* **574**, 501–504 (2019).
11. Hsu, C. W. *et al.* Observation of trapped light within the radiation continuum. *Nature* **499**, 188–191 (2013).
12. Gomis-Bresco, J., Artigas, D. & Torner, L. Anisotropy-induced photonic bound states in the continuum. *Nat. Photonics* **11**, 232–236 (2017).
13. Rybin, M. V. *et al.* High-Q Supercavity Modes in Subwavelength Dielectric Resonators. *Phys. Rev. Lett.* **119**, 1–5 (2017).
14. Vicencio, R. A. *et al.* Observation of Localized States in Lieb Photonic Lattices. *Phys. Rev. Lett.* **114**, 245503 (2015).
15. Baumberg, J. J., Aizpurua, J., Mikkelsen, M. H. & Smith, D. R. *Extreme nanophotonics from ultrathin metallic gaps*. *Nature Materials* vol. 18 668–678 (Nature Publishing Group, 2019).
16. Chikkaraddy, R. *et al.* Single-molecule strong coupling at room temperature in plasmonic nanocavities. *Nature* **535**, 127–130 (2016).
17. Benz, F. *et al.* Single-molecule optomechanics in ‘picocavities’. *Science (80-. )*. **354**, 726–729 (2016).
18. Leng, H., Szychowski, B., Daniel, M. C. & Pelton, M. Strong coupling and induced transparency at room temperature with single quantum dots and gap plasmons. *Nat. Commun.* **9**, 1–7 (2018).

19. Yoo, D. *et al.* Ultrastrong plasmon–phonon coupling via epsilon-near-zero nanocavities. *Nat. Photonics* 1–6 (2020) doi:10.1038/s41566-020-00731-5.
20. Mueller, N. S. *et al.* Deep strong light–matter coupling in plasmonic nanoparticle crystals. *Nature* **583**, 780–784 (2020).
21. Ciuti, C., Bastard, G. & Carusotto, I. Quantum vacuum properties of the intersubband cavity polariton field. *Phys. Rev. B - Condens. Matter Mater. Phys.* **72**, 115303 (2005).
22. Kockum, A. F. Ultrastrong coupling between light and matter. *Nat. Rev. Phys.* **1**, (2019).
23. Savage, K. J. *et al.* Revealing the quantum regime in tunnelling plasmonics. *Nature* **491**, 574–577 (2012).
24. Santhosh, K., Bitton, O., Chuntunov, L. & Haran, G. Vacuum Rabi splitting in a plasmonic cavity at the single quantum emitter limit. *Nat. Commun.* **7**, 1–5 (2016).
25. Kelly, K. L., Coronado, E., Zhao, L. L. & Schatz, G. C. The optical properties of metal nanoparticles: The influence of size, shape, and dielectric environment. *J. Phys. Chem. B* **107**, 668–677 (2003).
26. Dubrovkin, A. M. *et al.* Resonant nanostructures for highly confined and ultra-sensitive surface phonon-polaritons. *Nat. Commun.* **11**, 1–7 (2020).
27. Wang, T., Li, P., Hauer, B., Chigrin, D. N. & Taubner, T. Optical Properties of Single Infrared Resonant Circular Microcavities for Surface Phonon Polaritons. *Nano Lett.* **13**, 5051–5055 (2013).
28. Dunkelberger, A. D. *et al.* Active Tuning of Surface Phonon Polariton Resonances via Carrier Photoinjection. *Nat. Photonics* **12**, 1–8 (2017).
29. Kuttge, M., García De Abajo, F. J. & Polman, A. Ultrasmall mode volume plasmonic nanodisk resonators. *Nano Lett.* **10**, 1537–1541 (2010).
30. Epstein, I. *et al.* Far-field excitation of single graphene plasmon cavities with ultracompressed mode volumes. *Science (80-. )*. **368**, 1219–1223 (2020).
31. Brar, V. W., Jang, M. S., Sherrott, M., Lopez, J. J. & Atwater, H. A. Highly Confined Tunable Mid-Infrared Plasmonics in Graphene Nanoresonators. *Nano Lett.* **13**, 2541–2547 (2013).
32. Nikitin, A. Y. *et al.* Real-space mapping of tailored sheet and edge plasmons in graphene nanoresonators. *Nat. Photonics* **10**, 239–243 (2016).
33. Wang, S. *et al.* Metallic Carbon Nanotube Nanocavities as Ultracompact and Low-loss Fabry-Perot Plasmonic Resonators. *ACS Appl. Mater. Interfaces* **20**, 16 (2020).
34. Yang, X., Yao, J., Rho, J., Yin, X. & Zhang, X. Experimental realization of three-dimensional indefinite cavities at the nanoscale with anomalous scaling laws. *Nat. Photonics* **6**, 450–454 (2012).
35. Indukuri, S. R. K. C., Bar-David, J., Mazurski, N. & Levy, U. Ultrasmall Mode Volume Hyperbolic Nanocavities for Enhanced Light–Matter Interaction at the Nanoscale. *ACS Nano* **13**, 11770–11780 (2019).
36. Mock, J. J., Barbic, M., Smith, D. R., Schultz, D. A. & Schultz, S. Shape effects in plasmon resonance of individual colloidal silver nanoparticles. *J. Chem. Phys.* **116**, 6755–6759 (2002).
37. Yang, J. *et al.* Ultrasmall metal-insulator-metal nanoresonators: impact of slow-wave effects on the quality factor. *Opt. Express* **20**, 16880 (2012).

38. Tamagnone, M. *et al.* Ultra-confined mid-infrared resonant phonon polaritons in van der Waals nanostructures. *Sci. Adv.* **4**, eaat7189 (2018).
39. Caldwell, J. D. *et al.* Sub-diffractive volume-confined polaritons in the natural hyperbolic material hexagonal boron nitride. *Nat. Commun.* **5**, 5221 (2014).
40. Brown, L. V. *et al.* Nanoscale Mapping and Spectroscopy of Nonradiative Hyperbolic Modes in Hexagonal Boron Nitride Nanostructures. *Nano Lett.* **18**, 1628–1636 (2018).
41. Dolado, I. *et al.* Nanoscale Guiding of Infrared Light with Hyperbolic Volume and Surface Polaritons in van der Waals Material Ribbons. *Adv. Mater.* **32**, 1906530 (2020).
42. Alfaro-Mozaz, F. J. *et al.* Nanoimaging of resonating hyperbolic polaritons in linear boron nitride antennas. *Nat. Commun.* (2017) doi:10.1038/ncomms15624.
43. Autore, M. *et al.* Boron nitride nanoresonators for Phonon-Enhanced molecular vibrational spectroscopy at the strong coupling limit. *Light Sci. Appl.* **7**, 17172–17178 (2018).
44. Giles, A. J. *et al.* Imaging of Anomalous Internal Reflections of Hyperbolic Phonon-Polaritons in Hexagonal Boron Nitride. *Nano Lett.* **16**, 3858–3865 (2016).
45. Ambrosio, A. *et al.* Mechanical Detection and Imaging of Hyperbolic Phonon Polaritons in Hexagonal Boron Nitride. *ACS Nano* **11**, 8741–8746 (2017).
46. Lee, I.-H. *et al.* Pushing the polariton confinement limits with low losses using image polaritons in boron nitride. (2020).
47. Tamagnone, M. *et al.* High quality factor polariton resonators using van der Waals materials. (2019).
48. Basov, D. N. & Fogler, M. M. Hamiltonian Optics of Hyperbolic Polaritons in Nanogranules. (2015) doi:10.1021/acs.nanolett.5b00814.
49. Fisher, R. K. & Gould, R. W. Resonance cones in the field pattern of a short antenna in an anisotropic plasma. *Phys. Rev. Lett.* **22**, 1093–1095 (1969).
50. Low, T. *et al.* Polaritons in layered 2D materials. *Nat. Mater.* **16**, 1610.04548 (2017).
51. Date, P., Basov, D. N., Fogler, M. M. & Garcia de Abajo, F. J. Polaritons in van der Waals materials. *Science (80-. )*. **354**, aag1992–aag1992 (2016).
52. Sheinfux, H. H. *et al.* Evolution and reflection of ray-like excitations in hyperbolic dispersion media. *arXiv* (2021).
53. Caldwell, J. D. *et al.* Sub-diffraction, Volume-confined Polaritons in the Natural Hyperbolic Material, Hexagonal Boron Nitride. *Nat. Commun.* **5**, 5221 (2014).
54. Alfaro-Mozaz, F. J. *et al.* Nanoimaging of resonating hyperbolic polaritons in linear boron nitride antennas. *Nat. Commun.* **8**, (2017).
55. Lee, I.-H. H. *et al.* Image polaritons in boron nitride for extreme polariton confinement with low losses. *Nat. Commun.* **11**, (2020).
56. Dai, S. *et al.* Tunable phonon polaritons in atomically thin van der Waals crystals of boron nitride. *Science (80-. )*. **343**, 1125–1129 (2014).
57. Giles, A. J. *et al.* Ultralow-loss polaritons in isotopically pure boron nitride. *Nat. Mater.* **17**, 134–139 (2018).
58. Torre, I., Orsini, L., Ceccanti, M., Herzig Sheinfux, H. & Koppens, F. H. L. Green's functions

- theory of nanophotonic cavities with hyperbolic materials. *arXiv* (2021).
59. Silveirinha, M. G. Trapping light in open plasmonic nanostructures. *Phys. Rev. A - At. Mol. Opt. Phys.* **89**, 1–10 (2014).
  60. Liu, S. *et al.* Single Crystal Growth of Millimeter-Sized Monoisotopic Hexagonal Boron Nitride. *Chem. Mater.* **30**, 6222–6225 (2018).
  61. footnote - We note that the measured spectral data should be interpreted with some caution since due to technical limitation of the measurement technique only the real part of signal is measured, and a Lorentzian distribution, in the absolute value, can .
  62. Lyu, B. *et al.* Phonon Polariton-assisted Infrared Nanoimaging of Local Strain in Hexagonal Boron Nitride. *Nano Lett.* **19**, 1982–1989 (2019).
  63. Schmidt, P. *et al.* Nano-imaging of intersubband transitions in van der Waals quantum wells. *Nat. Nanotechnol.* **13**, 1035–1041 (2018).
  64. Verma, V. B. *et al.* Single-photon detection in the mid-infrared up to 10 micron wavelength using tungsten silicide superconducting nanowire detectors. (2020).
  65. Reserbat-Plantey, A. *et al.* Quantum Nanophotonics in Two-Dimensional Materials. *ACS Photonics* vol. 8 85–101 (2021).
  66. Zhang, H., Liu, Y.-C., Wang, C., Zhang, N. & Lu, C. Hybrid photonic-plasmonic nano-cavity with ultra-high Q/V. *Opt. Lett.* **45**, 4794 (2020).

# Figures

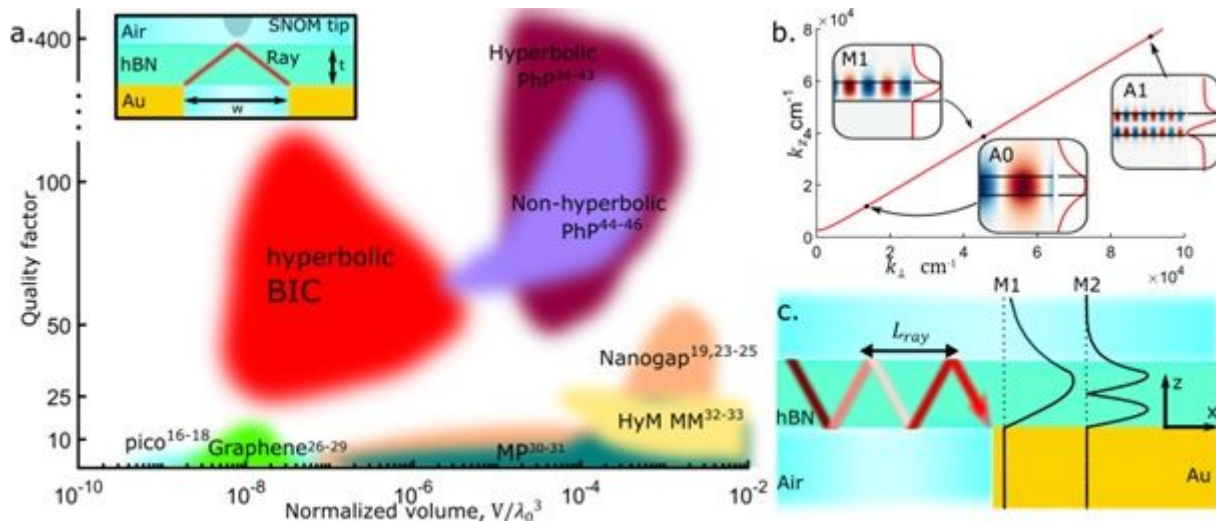


**Figure 1**

Overview of nanocavity and HyM physics. a. Survey of quality factor and normalized cavity volume (normalized by the vacuum photon volume) in various types of cavities and the ones reported here. Colored areas correspond to different cavity types: picocavities (pico), nanogap plasmon polaritons (nanogap), graphene plasmon polaritons (graphene), metallic particles (MP), hyperbolic metamaterials (HyM MM), non-hyperbolic phonon polaritons and hyperbolic phonon polaritons. Hybrid cavities, i.e. plasmonic structures embedded in macro-optical resonators can show higher quality factors at relatively large volumes<sup>66</sup>, but are not shown. Generally, cavities with  $V$  below  $10^6 \text{ nm}^3$  show low quality factors, typically below 10, and always below 20. See also extended details in SI. Inset shows a schematic of an hBIC cavity, with a ray-like excitation (red) and a nearby near field microscope tip. b. The isofrequency line in momentum space for h11BN at  $\omega = 1505 \text{ cm}^{-1}$ . The black dots show the location of the PhP eigenmodes A0, A1 and M1 associated to a 55nm thick flake. The PhP ray propagating in the hBN consists of a superposition of the eigenmodes A0, A1, A2,... The Insets show the calculated electric field distribution and profile of these eigenmodes. c. Illustration of ray propagation and reflection mechanism from a single cavity wall. The alternating color of the ray represents the phase of the ray, which increases at discrete jumps at every reflection from the top/bottom surfaces of the hBN. At the cavity wall, the overlap of the ray with the M<sub>1</sub>, M<sub>2</sub> modes (intensity profiles shown on the right) is minimal if the ray impinges exactly at the corner, leading to enhanced reflection.

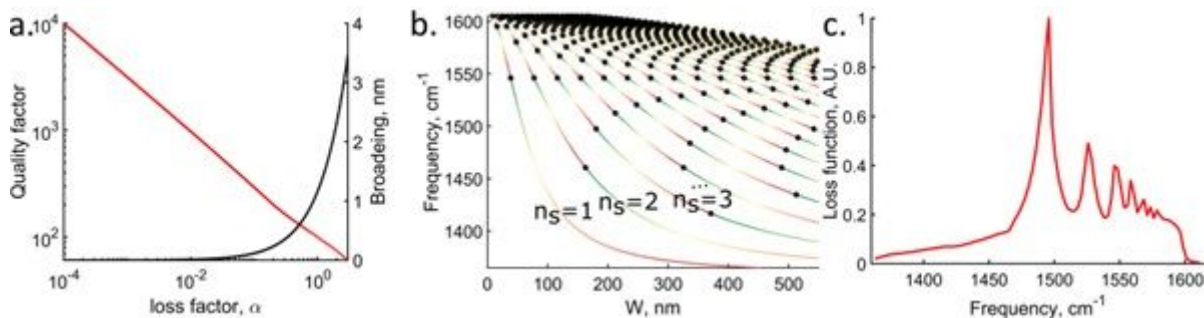


## Figure 2

Hyperbolic bound state in continuum cavities. a. Red line shows the analytical estimate of the quality factor as a function loss factor (a number multiplying the imaginary part of the the model permittivity)The black line shows the broadening, in nm, incurred for a ray in one skip inside the cavity. b. Conditions for hBIC formation. The solid lines are labeled by an integer  $n_s$ , which is the number of skips the ray makes inside the cavity (e.g.,  $n_s=1$  for Fig. 2a). The color of the line indicates phase accumulated in one roundtrip inside the cavity and the black dots indicate the frequency and cavity width for which a  $2\pi m$  phase is accumulated (for  $m \in \mathbb{N}$ ) and an hBIC can form. For example, the top left dot is a 1-skip cavity in which a  $2\pi$  phase is accumulated and in the top row of dots  $m=n_s$ , whereas other dots correspond to different values of  $m/n_s$  fractions c. Semi-analytical calculation of the loss function<sup>58</sup> in a 100nm wide cavity below a 25nm thick flake.

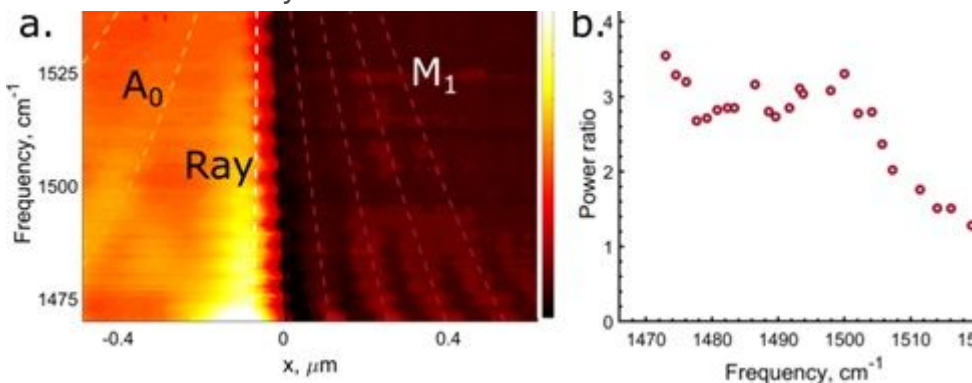


## Figure 3

SNOM measurements of ray and mode reflections. a. SNOM signal from PhPs of hBN that is placed on top of gold with a milled trench. The edge of the trench is at position  $X=0$ , with metal below the hBN for  $x>0$ . The trench is 800 nm wide and only the right half is shown, with the border indicated by the solid black line. The measurement shows a very strong fringe associated with the ray-like excitation and relatively faint fringes associated with M1 and A0. The dashed white line indicates the fitted location of the M1 fringes. The dashed green and red lines show the calculated location of the A<sub>0</sub> fringes and of the ray-like excitation which reaches from the top of the flake to the metallic corner, in good agreement with experimental observation. b. Normalized ratio of the amplitude of the ray-like fringe to the first fringe on the metal side. This asymmetry cannot be explained if multimodal effects are not considered.

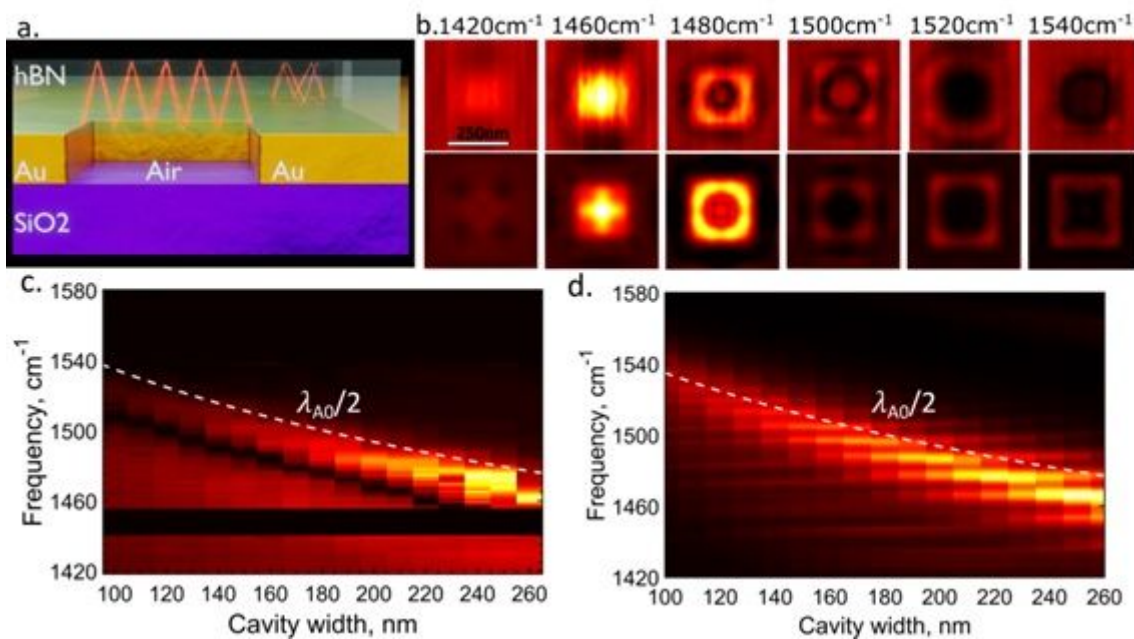


**Figure 4**

SNOM measurements of the hBIC cavities. a. Illustration of two cavities and ray-like excitations in them. b. Measured (top) and simulated (bottom) field distribution of a single square-shaped cavity (250nm $\times$ 250nm) at several frequencies. c.&d. Measured and simulated near-field signal in the middle of the cavity as a function of frequency and cavity size. The dashed white line on the experimental plot shows the expected first order resonance of the cavity. The undulations in the simulations are linked to multimodal beating interference, which in limit of lowering losses is expected to turn into an hBIC with  $ns \approx 2-3$ .

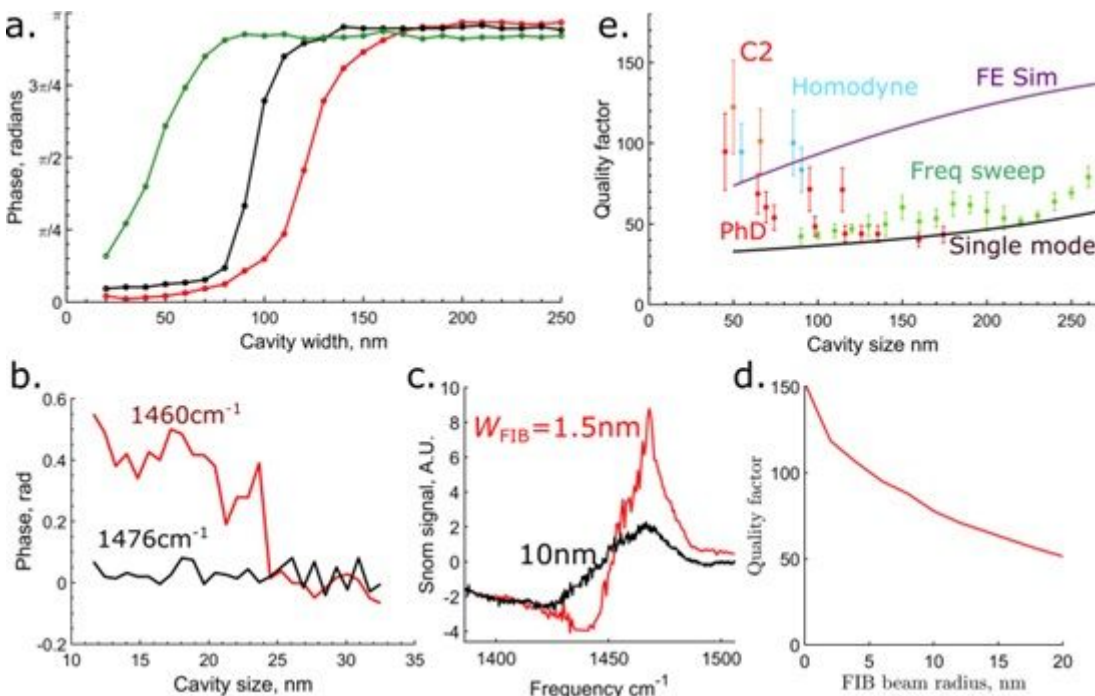


**Figure 5**

Quantifying cavity quality factors. a. Measured SNOM phase as a function of cavity width for cavity C1 (25nm thick hBN flake), showing a  $\pi$  phase-jump across the resonance. b. Similar measurement, but for a 3nm thick flake and for a set of smaller cavities. The on-resonance signal (red line taken at 1460  $\text{cm}^{-1}$ ) shows a clear phase-jump, in clear contrast with the off-resonance signal (black line, at 1476  $\text{cm}^{-1}$ ). Note that the phase-jump is smaller than  $\pi$ , due to coupling inefficiency and averaging because of the small cavity size in comparison with the SNOM tip apex. c. Spectral response of two cavities, one milled with a sharply focused FIB beam (1.5nm radius spot size) and the other intentionally broadened (10nm radius). d. Simulated quality factor in cavities as a function of the milling beam's radius. e. Quality factor vs. cavity width measured in our experiment. The solid black line shows the theoretical upper-bound limit that can be attained by neglecting higher order modes and the purple line is a finite element simulation that includes the ray-like propagation and reflection. The measured values have been extracted by three different type of measurements (see SI): frequency sweeps (green), pseudoheterodyne scans (red for cavity set C1 and orange for cavity set C2) and homodyne amplitude scans (light blue). Different extraction methods are in general agreement and in all cases exceed the single mode theory. Theory and simulations are for a 25nm h11BN flake, similar to cavity set C1.

## Supplementary Files

This is a list of supplementary files associated with this preprint. Click to download.

- [HBCSI4f.docx](#)